ARTICLE OPEN

Check for updates

# Coupled mixed-potential and thermal-hydraulics model for long-term corrosion of copper canisters in deep geological repository

Nakkyu Chae[1], Samuel Park[1], Seungjin Seo[1], Richard I. Foster[2], Heejae Ju[3] and Sungyeol Choi[1,2,4]✉

Canister performance is a major issue for constructing reliable deep geological repositories for storing spent nuclear fuels, and corrosion resistance is main the factor determining canister durability. We developed a 2-D multiphysics model, which can predict both the corrosion rate and potential, for simulating copper canister corrosion in deep geological repositories. We found that canisters corroded through the long-cell action in a deep geological repository, the corrosion was quite limited, and the overall canister durability was around 1.7 million years. Our results demonstrated that copper exhibits sufficient corrosion resistance and that long-cell action-based corrosion cannot severely damage copper canisters.

*npj Materials Degradation* (2023)7:26 ; https://doi.org/10.1038/s41529-023-00345-6

## INTRODUCTION

Deep geological repositories (DGRs) are the final resting place for nuclear fuels after being burned in nuclear reactors for almost all types of nuclear fuel cycles[1–5]. The concept of a DGR is to bury spent nuclear fuels (SNF) under several hundred meters below the ground surface. The purpose of DGRs is isolation of spent nuclear fuels until the radiotoxicity of spent nuclear fuels decays to the radiotoxicity level of natural uranium ore, thus minimizing the burden for future generation. DGRs do not need any operators or managements after closure.

After the closure of DGRs, the DGRs will not be managed by humans and must isolate the spent nuclear fuels for several million years. Hence, a multiple physical barrier concept is applied to DGRs. A DGR consists of disposal tunnels, a natural barrier, and engineering barriers (Fig. 1). The tunnels are paths for stored spent nuclear fuels in DGR. The natural barrier is one of the protective layers to isolate spent nuclear fuels and it is host rock which varies with sites for DGR. Engineering barriers consist of the canisters, bentonite, and backfill material. Spent nuclear fuels are encapsulated in the canister and disposed into disposal holes. The bentonite fills the gap between canister and disposal hole (host rock), and backfill material fills the disposal tunnels after disposing of canisters in the disposal holes to minimize any mass transportation through gaps.

Because SNF storage canisters can fail over geological time scales, the long-term corrosion of canisters in deep geological repositories (DGRs) is an important factor to consider when designing DGR systems[6–11]. Such failures would release highly radioactive waste, which would pose considerable radiotoxicity and environmental risks. Hence, because copper exhibits good corrosion resistance to underground environmental conditions, it is a suitable candidate material for manufacturing corrosion-resistant canisters[6,12–14]. However, although, copper exhibits good corrosion resistance, it can be corroded by oxygen and sulfide species in DGRs[6,14,15]. Therefore, because copper cannisters must be durable over geological time scales (i.e., from thousands of to several million years), copper canister corrosion must still be evaluated under DGR conditions. However, owing to the time-frames required to fully elucidate canister corrosion, conventional physicochemical approaches for studying corrosion are limited.

Because geological time scales are impossible to experimentally simulate and similar natural analogs are difficult to find, computational modeling is the only method for calculating and predicting canister lifetimes[16–18]. Extensive research has been conducted to develop numerical codes for studying the long-term corrosion of canisters under various DGR oxic and anoxic conditions[8,19–26]. For instance, King used mixed-potential theory and a unidimensional code to develop a copper sulfide model (CSM)[20], which can predict the effects of complex chemical reactions on the copper corrosion and corrosion potential of canisters in DGRs. However, CSM cannot consider and analyze the effect of host rock fracture networks on corrosion by coupling of different dominant redox reactions on different surfaces of Cu canisters[20,27]. In contrast, the Nuclear Waste Management Organization (NWMO) used COMSOL Multiphysics® software to develop a 3-D corrosion model for studying canister corrosion in DGRs[21,22,24,28]. Although this 3-D COMSOL model can calculate the effect of fracture networks on copper corrosion, it cannot predict the corrosion potential and any chemical reaction effects owing to boundary condition assumptions.

Although extensive research has been conducted using computational modelling to study the long-term corrosion of copper canisters, the models are limited because they either do not consider the effect of host rock fracture networks (coupling of different dominant redox reactions on surfaces of canister) on corrosion or cannot predict the corrosion potential and any chemical reaction effects owing to boundary condition assumptions. Therefore, we coupled mixed-potential theory and thermal hydraulics to develop a flexible model (applicable in 3-D) for simulating corrosion processes in 2-D and predicting the corrosion potential and effects of the host rock fracture networks on the copper canister corrosion. Moreover, we compared the corrosion

[1]Department of Nuclear Engineering, Seoul National University, 1 Gwanak-ro, Gwanak-gu, Seoul 08826, Republic of Korea. [2]Nuclear Research Institute for Future Technology and Policy, Seoul National University, 1 Gwanak-ro, Gwanak-gu, Seoul 08826, Republic of Korea. [3]Korea Atomic Energy Research Institute, 111 Daedeok-daero, Yuseong-gu, Daejeon 34057, Republic of Korea. [4]Institute of Engineering Research, Seoul National University, 1 Gwanak-ro, Gwanak-gu, Seoul 08826, Republic of Korea. ✉email: choisys7@snu.ac.kr

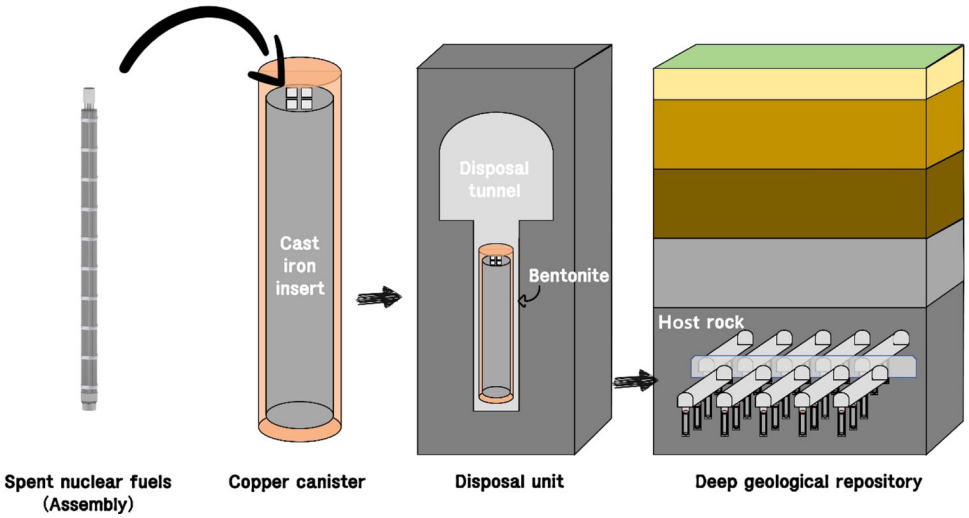


**Fig. 1 Conceptual design of deep geological repository.** Schematic diagram of a deep geological repository system and its multibarrier (engineering and natural barriers).

potential and Cu sulfidation layer thickness for up to 1750 h (experimentally reported data from Chen et al. 2010 and 2017) to validate the model for both copper corrosion and corrosion depth with experimentally reported data and, used the model to analyze the effects of the corrosion fractures, engineering barrier (i.e., disposal hole and tunnel), and host rock interface on the long-term canister corrosion[29–31]. The results suggested that the model could be used to analyze both long-term local corrosion and copper durability.

## RESULTS AND DISCUSSION

### Validation of model: corrosion potential

Figure 2 shows the results of the first model validation dataset for simulating the corrosion potentials of the $O_2$-free, constant $O_2$, and $O_2$ consumption Cu corrosion models. The corrosion potential of the $O_2$-free specimen was simulated without using an initial $O_2$ concentration. The corrosion potentials of the constant $O_2$ and $O_2$ consumption models were simulated using an initial $O_2$ concentration of 22 μM. The initial $O_2$ concentration was calculated from the initial corrosion potential −0.335 $V_{SCE}$ from the experiment of Smith et al.[32]. In the case of constant $O_2$, $O_2$ is not consumed by the reduction of $O_2$ reaction with Cu, in contrast, in the $O_2$ consumption case, the $O_2$ is consumed by the reduction reaction of $O_2$ with Cu. The total added $HS^-$ concentration is also plotted in Fig. 2. In the experiment of Smith et al., $HS^-$ was added gradually to the solution after reaching the stable corrosion potential in the experiment[32]. Scatter points represent the experimentally measured data by Smith et al.[32].

Among the three models, which are the $O_2$ free, constant $O_2$, and $O_2$ consumption models, the $O_2$ consumption model shows quite similar simulated results with the experimental data (scatter data in Fig. 2). At the beginning of the experiment (Smith et al.), the Cu specimens were stored in water with a low concentration of $O_2$ which shows −0.335 $V_{SCE}$ corrosion potential (~50 min)[32]. Except for the $O_2$ free model, the other two models show the very similar result with the experimental data until 200 min. At the beginning of the experiments, even though a very small concentration of $HS^-$ was added (3.32E-5M), the corrosion potential dropped significantly ~0.42 V for both experiment and the numerical results (Constant $O_2$ and $O_2$ consumption models). For the $O_2$-free model, the simulated corrosion potential was lower than the experimentally measured one in the range of 0–200 min due to the absence of $O_2$ in the solution.

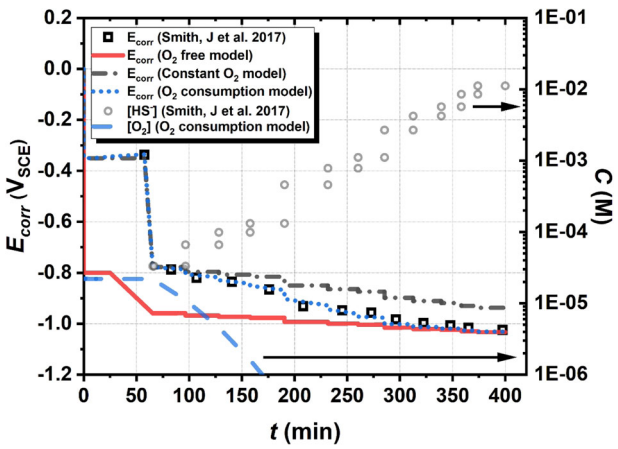


**Fig. 2 Validation of simulated corrosion potential with experimental data.** Comparison of experimentally measured by Smith et al. and numerically simulated corrosion potentials ($E_{corr}$) of copper specimens immersed in solutions containing different $HS^-$ concentrations, the left *y*-axis stands for corrosion potential ($V_{SCE}$) and right *y*-axis stands for $O_2$ and $HS^-$ concentration[32].

After 200 min, the $O_2$ free model and $O_2$ consumption model show similar corrosion potential to the experimental data, but the constant $O_2$ model deviated from the experimentally measured data. This trend change can be explained by the $O_2$ concentration in the solution from the calculated results $O_2$ consumption model. As can be seen in Fig. 2, the concentration of $O_2$ consumed and lower than below 1 uM after 175 min from the $O_2$ consumption model. Therefore, the $O_2$ concentration became negligibly small and did not affect the corrosion potential for relatively longer corrosion after 200 min. The $O_2$-free model did not imply any $O_2$, so after 200 min, the corrosion potential is similar to the experimental data. However, the $O_2$ constant model maintains the concentration of $O_2$ at 22 μM and the corrosion potential was slightly overestimated than the experimental data.

We can highlight that the early corrosion potential (up to 200 min) follows mixed-potential theory for which the $O_2$ and $HS^-$ both contribute to overall corrosion potential. However, as suggested by Smith, J. et al., the $HS^-$ concentration increased, the corrosion potential is lowering to a negative potential, and the corrosion potential is getting closer to the equilibrium potential of

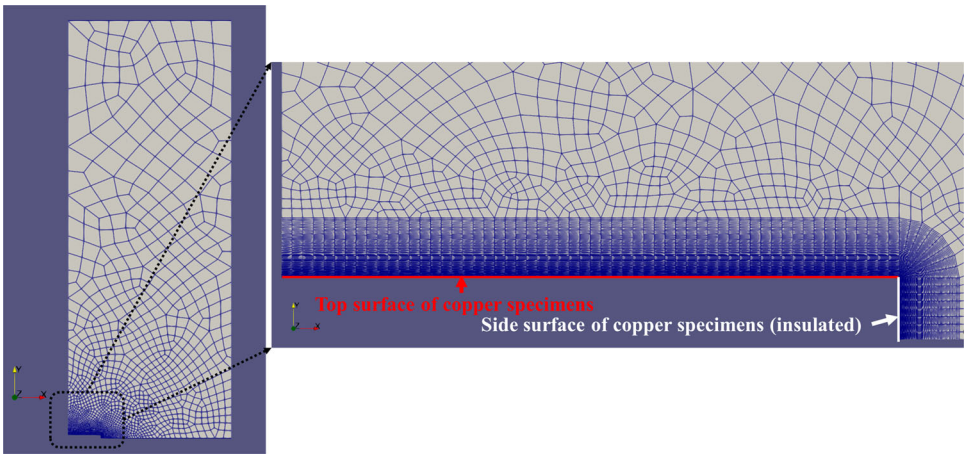


**Fig. 3 Geometry for simulated corrosion of Cu.** Simplified 2-D geometry for simulating corrosion of Cu immersed in 1 L of solution containing both $HS^-$ and $Cl^-$ ions.

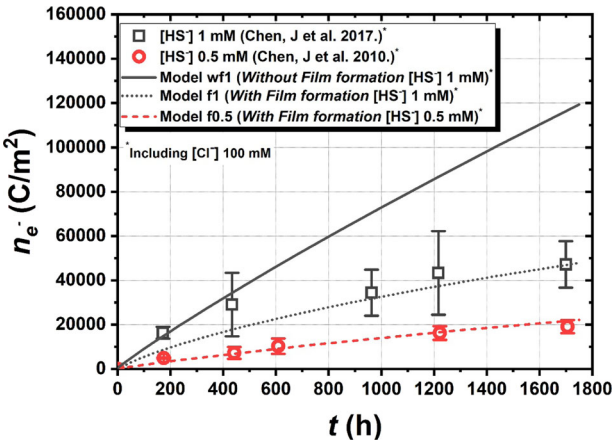


**Fig. 4 Validation for simulated amounts of corroded Cu.** Comparison of data experimentally measured by Chen et al. (2010 and 2017) and numerically simulated in this study corroded amounts of Cu in terms of number of electrons per unit area ($n_e^-$) for Cu immersed in 0.1 M $Cl^-$ with 1 mM $HS^-$ and 0.5 mM $HS^-$ solutions[29,30].

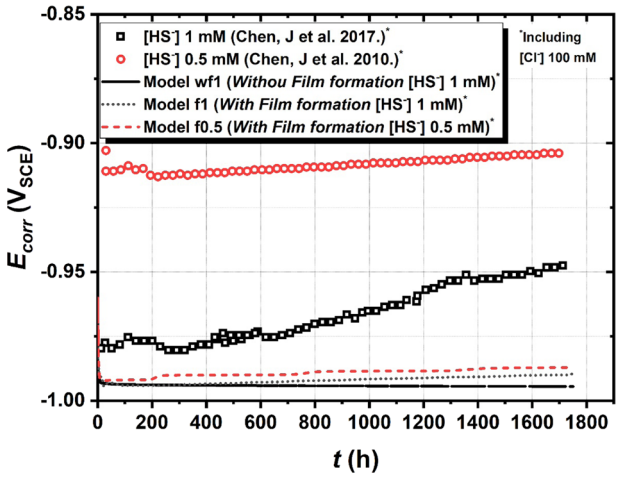


**Fig. 5 Validation of simulated corrosion potential with experimental data.** Comparison of data experimentally measured by Chen et al. (2010 and 2017) and numerically simulated in this study for corrosion potential ($E_{corr}$) of Cu immersed in 0.1 M $Cl^-$ with 1 mM $HS^-$ and 0.5 mM $HS^-$ solutions[29,30].

the $Cu/Cu_2S$ reaction[32]. Hence, the overall corrosion potential depends on $HS^-$ only after significant consumption of $O_2$.

By comparing the suggested models with experimental data, the following effects can be expected in the DGR conditions. First, the corrosion potential of Cu can be significantly dropped from the aerobic condition to the anaerobic condition. Second, in the early stage of DGR (aerobic to transient periods for anaerobic conditions), corrosion potential will be decided by mixed-potential theory, but in the anaerobic conditions $HS^-$ will be dominant and the overall corrosion potential will be similar to the equilibrium potential of $Cu/Cu_2S$ reaction. These effects are observed in the results of the DGR model section.

### Validation of model: amounts of corroded Cu

For the second dataset, previously reported experimentally measured data were used to validate the model for amounts of corroded Cu and corrosion potential, which are the most important factors for Cu corrosion under DGR conditions[29]. A 2-D geometry (Fig. 3) was used to calculate the corrosion potential and the amounts of corroded Cu. Figures 4 and 5 show the experimentally measured and numerically calculated the amounts of corroded Cu in the terms of electrons per unit area and corrosion potentials, respectively. The electrons per unit area unit means how much Cu lost its electron and is equivalent to the number of corroded Cu atoms because Cu is corroded to $Cu^+$ ($Cu_2S$).

**Table 1.** Summary of three corrosion models for $HS^-$ and $Cl^-$ solutions.

| Unit: mM | $HS^-$ | $Cl^-$ | $Cu_2S$ film growth |
|---|---|---|---|
| Model wf1 | 1 | 100 | X |
| Model f1 | 1 | 100 | O |
| Model f0.5 | 0.5 | 100 | O |

Figure 4 shows the results of the second model validation dataset for the simulating amounts of corroded Cu and corrosion potentials. A total of three different Cu corrosion models (Table 1) were calculated. Among the three models, two of them (Model wf1 and f1) were corrosion of Cu in $HS^-$ 1 mM (including $Cl^-$ 100 mM) solution with considering the formation of $Cu_2S$ film and without considering the formation of $Cu_2S$ film on the Cu surface. The remaining model (Model f0.5) simulated the Cu corrosion

model for $HS^-$ 0.5 mM and $Cl^-$ 100 mM solution with considering $Cu_2S$ film.

In the case of $HS^-$ 1 mM and $Cl^-$ 100 mM solution, the amounts of corroded Cu were similar until 600 h between the experimental data and the model wf1 (Black line in Fig. 4). However, after 600 h, the model wf1 overestimated the amount of corroded Cu. In the case of considering the film formation (Model f1 and Black dot line in Fig. 4), the model f1 shows quite well-matched results after 600 h with the experimental data. By comparing the two models (Model wf1 and f1 in Fig. 4), the model wf1 overestimated the film thickness after 600 h due to the absence of $Cu_2S$ film on the Cu surface. The model wf1 did not consider the film formation and there was no factor to retard the diffusion of $HS^-$ to the Cu surface. However, in the experiment and the model f1, the $Cu_2S$ film slows down the diffusion of $HS^-$ through the film and eventually affects to reaction rate (corrosion rate) of Cu. Hence, the graph of the experimentally measured $Cu_2S$ film thicknesses appeared parabolic, as shown in Fig. 4. This parabolic shape of the result can be observed in the film formation model results (model f1, Black dot line in Fig. 4) as well. Therefore, the overall corrosion rate is affected by the film formation of $Cu_2S$ for long-term corrosion in solution conditions.

The amounts of Cu corrosion in $HS^-$ 0.5 mM and $Cl^-$ 100 mM cases are very similar between the experiment results (Red scatter in Fig. 4) and the simulated results (Model f0.5, Red dash line in Fig. 4). Both results show parabolic shapes, but less parabolic than the 1 mM $HS^-$ case. Hence, the $HS^-$ 0.5 mM case also shows the effect of $Cu_2S$ film formation, but relatively weak due to the lower concentration of $HS^-$.

For the model f1 and model f0.5, the effective $HS^-$ diffusion coefficient was set to $3.6E-14\ m^2\ s^{-1}$, which was calculated using porosity and tortuosity of $5E-4$ and 0.1, respectively. The effective diffusion coefficient was quite low and comparable to the effective diffusion coefficient (between $1E-10$ and $1.2E-14\ m^2\ s^{-1}$) of $Cu^+$ ions in the $Cu_2S$ film[33]. According to Chen et al., $Cu_2S$ films grow outward, suggesting that $Cu_2S$ is deposited on other $Cu_2S$ layers[34]. Hence, this $Cu_2S$ film formation mechanism and the numerically calculated and experimentally measured results suggest that the $Cu_2S$ film growth was controlled by the Cu diffusion through the $Cu_2S$ films.

The corrosion potential of 1 mM $HS^-$ solution shows a similarity between the experiment and numerical model f1 results (agree within 0.05 $V_{SCE}$). In contrast, the low concentration of $HS^-$ solution (0.5 mM) shows more different corrosion potential (up to $-0.08$ $V_{SCE}$) between the experiment and model f0.5 results. Despite differences in numerical models and experimental data, the numerical models (model f1 and model f0.5) show similar corrosion potential trends with experimental data. For both corrosion potentials in 1 mM $HS^-$ and 0.5 mM $HS^-$ solutions, initial corrosion potentials move to a more negative way (or vibrate) and after around 400 h, start to move into more positive potentials.

These trends can be explained by two different terms which are the concentration of $O_2$ and the formation of $Cu_2S$ film. Figure 6 shows the contour of corrosion potential with the concentration of $HS^-$ and $O_2$ calculated by mixed-potential Eq. (1). In Fig. 6, corrosion potential positively increases as either increment of $O_2$ concentration or depletion of $HS^-$ concentration and negatively increases as decreasing of $O_2$ concentration or increasing of $HS^-$ concentration. At the beginning of corrosion in Fig. 5, the corrosion potentials are negatively increased due to depletion of $O_2$ concentration; because as can be seen in Fig. 6, physically decreasing $O_2$ is the only way to negatively increase of corrosion potential in the solution, unless adding more $HS^-$ in the solution. The case of increasing corrosion potential positively (experimentally around 200–400 h and numerically around 100 h) is due to film formation of $Cu_2S$ film on the Cu surface. Because the $Cu_2S$ film retard the diffusion of $HS^-$ from the bulk solution to the bare

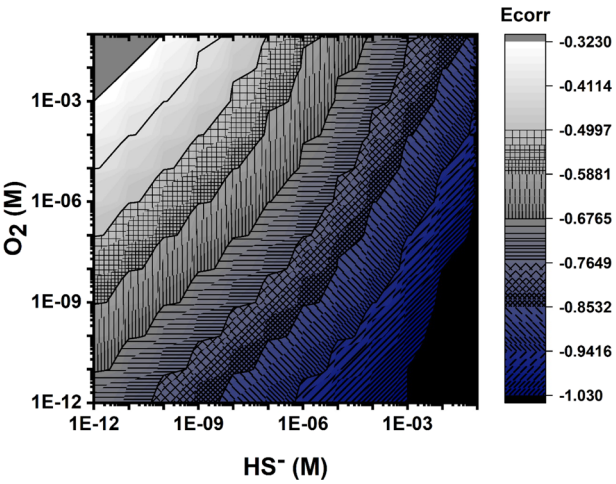


**Fig. 6 Simulated corrosion potential with variables.** Contour of corrosion potential ($E_{corr}$) with concentration of $HS^-$ and $O_2$ by mixed-potential Eq. (1).

Cu surface and eventually induce depletion of $HS^-$ on the Cu surface.

The beginning corrosion potentials are already quite different between the experimental data and the numerical model for $HS^-$ 0.5 mM solution. These initial corrosion potentials indicate that there could be some amounts of $O_2$ presented at the beginning of the experiment for $HS^-$ 0.5 mM solution in Chen et al.[29]. However, there is no detailed information about the initial concentration of $O_2$ in the $HS^-$ 0.5 mM solution (Chen et al.) and the model f0.5 applied the same initial $O_2$ concentration as the model f1. Also, as can be seen in Fig. 6, from 0 to μM level of $O_2$ can significantly change corrosion potential from at least $-1.03$ to $-0.853$ $V_{SCE}$ for a range of $HS^-$ 0.5–1 mM concentration. Therefore, the disagreement of corrosion potential could be originated from different concentrations of $O_2$ between the model f0.5 and the experimental data.

The numerical model was validated using two datasets, and the numerically simulated and experimentally measured data agreed well. Therefore, the numerical model was applied to the KAERI reference disposal unit. However, owing to the mesh size, the $Cu_2S$ film growth could not be applied to simulate the KAERI reference disposal unit, which requires the copper surface mesh size to be smaller than 1 μm. Because this is impractical to simulate owing to the high computational cost, the KAERI reference disposal unit was conservatively simulated using the model without the $Cu_2S$ film growth.

### Sensitivity of mesh quality

Mesh size is one of the most important parameters for modeling canister corrosion with the finite element method because a mesh that is too coarse can lead to huge errors in the chemical species (e.g., $HS^-$ and $O_2$ oxidant) flux on surfaces, which can underestimate the corrosion rate and depth. However, a mesh that is too fine would require a considerable computational cost. Hence, to check the mesh quality in the numerical model, we derived and used the following analytical solution:

$$J_{analytical} = D_0 \cdot \exp\left(-\frac{E_a}{RT}\right) \cdot \tau \cdot \varepsilon \cdot \frac{C_b - C_a}{a \cdot \ln(b/a)}, \quad (1)$$

where $J_{analytical}$ is the $HS^-$ flux [mol·m$^{-2}$ a$^{-1}$] on the canister surface, $D_0$ is the diffusion coefficient [mol·m$^{-2}$ a$^{-1}$] at 298.15 K, $E_a$ is the activation energy [−15000 J·mol$^{-1}$], $R$ is the ideal gas constant [8.314 J·K$^-$ mol$^{-1}$], $T$ is the temperature (K), $C_b$ is the concentration [mol·m$^{-3}$] of the bentonite outer surface, $C_a$ is the

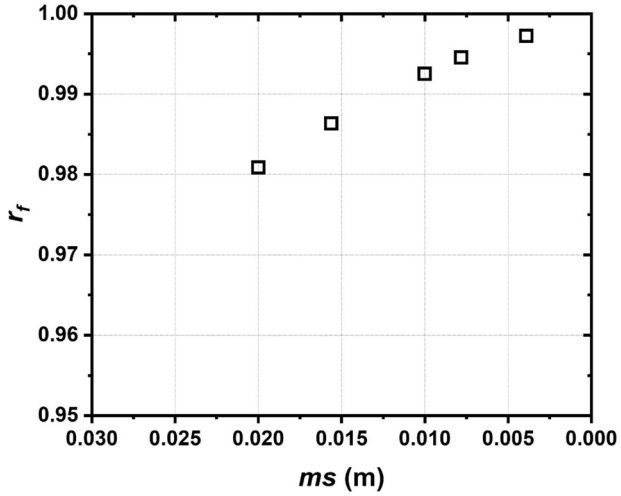


**Fig. 7 Comparison between analytical solution and numerical solution.** Relative flux ($r_f$) (= Numerically calculated flux × Analytically calculated flux$^{-1}$) of $HS^-$ on Cu canister surface, as calculated for different canister and bentonite surface mesh sizes.

concentration mol·m$^{-3}$ of the bentonite inner (canister) surface, $a$ is the canister radius [m], and $b$ is the bentonite block outer radius [m]. The analytical solution represented by Eq. (1) was derived for the $HS^-$ flux on the Cu canister surface, and the bentonite shape was assumed to be a hollow cylinder, which can represent the shape of the bentonite blocks exactly at the beside of the canisters.

The relative flux is given by

$$J_r = \frac{J_{\text{numerical}}}{J_{\text{analytical}}}, \quad (2)$$

where $J_r$ is the (dimensionless) relative $HS^-$ flux, $J_{\text{numerical}}$ is the numerically calculated $HS^-$ flux [mol·m$^{-2}$ a$^{-1}$] on the canister surface, and $J_{\text{analytical}}$ is the $HS^-$ flux [mol·m$^{-2}$ a$^{-1}$] on the canister surface, as calculated analytically using Eq. (1). The initial and boundary conditions and geometry used to calculate the flux numerically and analytically are given in Supplementary Methods. Figure 7 shows the relative fluxes calculated for different canister surface and bentonite mesh sizes. Clearly, the numerically and analytically calculated fluxes converged with decreasing mesh size. Compared to the analytically calculated flux, the flux numerically calculated using a mesh smaller than 0.01 m exhibited <1% error, which was small enough to calculate the $HS^-$ flux in the numerical model. Therefore, a 0.01 m mesh was used for the entire numerical model in this study.

### Fractures around engineering barriers: thermal hydraulics

Next, the KAERI reference disposal unit thermal hydraulics were analyzed. Specifically, the temperature and saturation degree were analyzed at the canister/bentonite and bentonite/host rock interfaces and compared with those measured using the KAERI model developed by Lee et al. as shown in Figs. 8 and 9[35]. The KAERI model has a good capability to predict the thermal-hydro-mechanical (THM) behavior of engineered barriers and natural barriers in the DGR. Also, the KAERI model did several validation cases for the THM behavior[35,36]. However, the KAERI model does not have a corrosion model. Hence, the KAERI model is a good comparable model with the developed corrosion model for the thermal-hydraulics behavior in the DGR. In Fig. 8, although the temperature profile of the bentonite/host rock interface measured in this study was quite like the temperature profile of the one measured by Lee, C. et al. the temperature profiles of the canister/bentonite interface were different for 10 years likely because we

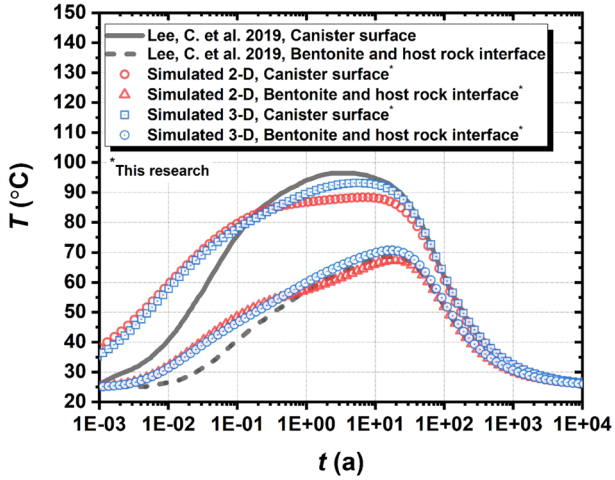


**Fig. 8 Validation of temperature profile.** Comparison of temperatures ($T$) between Lee et al. and our model for canister/bentonite and bentonite/host rock interfaces[35].

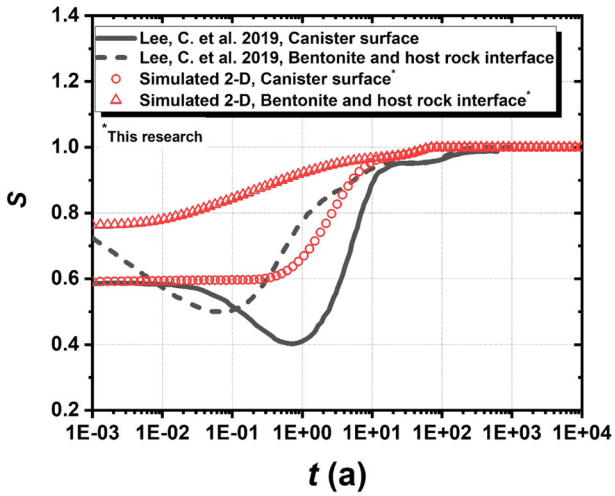


**Fig. 9 Validation for degree of saturation profile.** Comparison of degree of saturation ($S$) between Lee et al. and our model for canister/bentonite and bentonite/host rock interfaces[35].

used a 2-D model and Lee et al. used a 3-D one[35]. However, the maximum difference between both temperature profiles was approximately 8 °C, and both profiles exhibited the maximum temperature below 100 °C.

In Fig. 8, a developed 3-D model is presented to compare with the 2-D and the Lee et al. model. As can be seen in Fig. 8, the difference between the developed 3-D model and Lee et al. model is around 3 °C, which is quite a small value. The small temperature difference originated from the drying out of bentonite which induces the occurrence of an earlier maximum temperature and slightly higher maximum temperature.

The difference in the temperature profiles is unlikely to alter the Cu canister corrosion and cannot contribute to the copper canister lifetime because the temperature was only different for 10–20 years before it equilibrated, which is quite short compared to the simulation time scale (i.e., approximately 0.001% of the total simulation time). In addition, at approximately 10 years, the temperature near the canister was so high that the surrounding bentonite would likely dry out and be unable to maintain groundwater-induced corrosion. Instead, gaseous corrosion would occur much slower than groundwater-induced corrosion, which this model considered even under dry conditions. Also, the

simulated condition is the center of the DGR which means the maximum temperature of other positions would not be that high. Therefore, the model conservatively analyzed the corrosion depth and canister lifetime. In a future study, we will couple 3- and 2-D models to calculate the temperature profile for the mixed-potential model more accurately.

Figure 9 shows the degrees of bentonite saturation by water near the canister/bentonite and bentonite/host rock interfaces. Our numerical model and the one developed by Lee, C. et al. both showed that the bentonite would be fully saturated with water after approximately 100 years. Although the model developed by Lee et al. showed that the bentonite would dry out owing to water evaporation in the bentonite, our numerical model did not consider water evaporation. Water can evaporate with rising bentonite temperature owing to the heat generated from decaying spent nuclear fuels. To simulate this effect, models should consider both water flow and evaporation. However, because our model only considered the water flow, the bentonite did not dry out, which is why the profile generated using our model was different from the one generated using the model developed by Lee et al. In future work, we will develop and implement water evaporation in the numerical model. The authors found Richard's flow can be a good method to incorporate water evaporation in bentonite with slightly increasing computational time.

### Fractures around engineering barriers: corrosion potentials

The canister corrosion potential was analyzed over time, as shown in Fig. 10. The corrosion potential dropped from −0.285 $V_{SCE}$ at the beginning of the simulation (0.1 year) to −0.96 $V_{SCE}$ after 100 years. The initial corrosion potential (between −0.285 and −0.3 $V_{SCE}$) showed that the corrosion proceeded under oxic conditions. After 100 years, the corrosion potential remained unchanged at

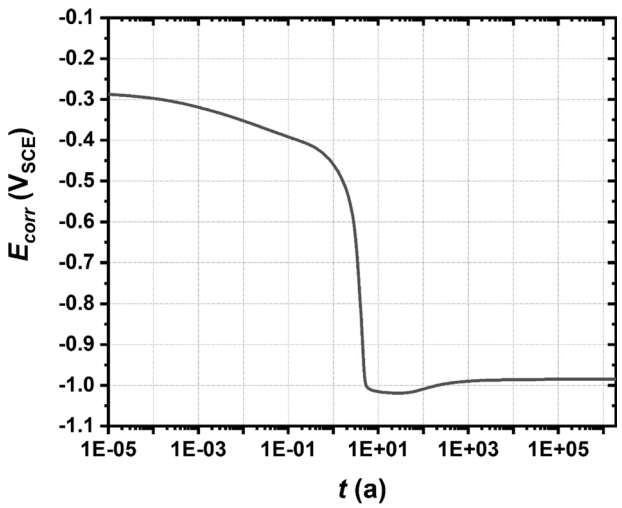


**Fig. 10 Simulated corrosion potential for deep geological repository.** Corrosion potential ($E_{corr}$) of Cu canister.

−0.94 $V_{SCE}$, which was relatively higher than the equilibrium potential of −1.04 $V_{SCE}$ for reaction B in Table 2 ($Cu_2S$/Cu)[32]. This deviation from the equilibrium potential originated from the sulfide depletion on the canister surface, which reaction kinetics were much faster than those of the sulfide transportation in the bentonite. This trend agreed with the accepted mechanism wherein sulfide ion diffusion controls copper corrosion[37].

$O_2$ was supplied on the top surface of the canister for a prolonged period because $O_2$ remained in tunnel (Fig. 11). In contrast, $HS^-$ (Fig. 12) was supplied faster on the side of the canister. These $O_2$ and $HS^-$ distributions induced the distribution of anodic and cathodic currents, as shown in Fig. 13. Additionally, Fig. 13 shows the redox current distributions of each reaction, and the anodic and cathodic sites are separated as the top and side surfaces, respectively. On the side surface, the Cu was sulfidated to $Cu_2S$, and the electrons generated from the Cu were supplied to the top surface to reduce $O_2$.

Between 2 and 10 years (indicated by the gray square in Fig. 13), the canister corroded through the long-cell action. As shown in Fig. 13, from 2 to 10 years, $O_2$ was predominantly reduced on the top surface, which was the main electron donor. In contrast, the side surface exhibited much higher anodic currents, which means that the canister corroded much faster on the side copper surface. Therefore, between 2 and 10 years, the canister corroded through the long-cell action, and the copper corrosion was accelerated on the side surfaces.

Figure 14 shows the total corrosion depths at the top and bottom corners, which are the most corroded positions of the copper canister. Calculation results are presented for the $O_2$-containing (e.g., bentonite and backfill) and -free engineering barrier systems. The $O_2$-free engineering barrier system did not corrode through the long-cell action. As shown in Fig. 14, although the copper canister corrosion was accelerated by the long-cell action for up to 100 years, the difference between the corrosion of the top and bottom corners was quite small: less than 1 μm. Therefore, the long-cell action negligibly affected the corrosion.

### Fractures around engineering barriers: local corrosion

The calculated corrosion potentials and redox current densities (shown in Figs. 10 and 13, respectively) indicated that the first hundred years were quite unstable and that oxic corrosion transitioned to anoxic corrosion. In addition, over the same period, the oxic and anoxic corrosion conditions varied for the different canister surfaces. Owing to the residual $O_2$ in the tunnel and upper bentonite blocks, the canister top surface may be more prone to pitting corrosion in $Cl^-$ solutions. However, the corrosion potential is below −0.29 $V_{SCE}$ were considerably lower than the pitting corrosion potentials in the range 0.4–0.9 $V_{SCE}$ (corresponding to pHs in the range 7.26–9.24) for the $O_2$ containing 0.1 M $Cl^-$ solution[38].

For the case of low $O_2$ (mixed oxic and anoxic corrosion condition) and anoxic corrosion condition, the pitting corrosion potentials are located between −0.05 to −0.40 $V_{SCE}$ for 0.1 to 5000 mM of $Cl^-$ and −0.20 to −0.05 VSCE for 0.1 to 100 mM of $Cl^-$

**Table 2.** Electrochemical and corresponding Butler–Volmer equations for Cu interfacial redox reactions under both oxic and anoxic conditions.

| | Electrochemical reaction | Butler–Volmer equation |
|---|---|---|
| A | $Cu + 2Cl^- \rightleftarrows CuCl_2^- + e^-$ | $i_A = Fn_A\{k_A C_1^2 \exp\frac{F}{RT}(E_{CORR} - E_A) - k_{AB}C_5\} * \text{Area}$, (4) |
| B | $2Cu + HS^- \rightleftarrows Cu_2S + H^+ + 2e^-$ | $i_B = Fn_B k_B C_2^2 \exp\left\{\frac{(1+a_{B1})F}{RT}E_{CORR}\right\}\exp\left\{-\frac{F}{RT}(E_{B1} + a_{B2}E_{B2})\right\} * \text{Area}$ (5) |
| C | $O_2 + 2H_2O + 4e^- \rightleftarrows 4OH^-$ | $i_C = -Fn_C k_C C_3 \exp\left\{-\frac{a_C F}{RT}(E_{CORR} - E_C)\right\} * \text{Area}$ (6) |
| E | $HS^- + H_2O + e^- \rightleftarrows \frac{1}{2}H_2 + HS^- + OH^-$ | $i_E = -Fn_E k_E C_2 \exp\left\{-\frac{a_E F}{RT}(E_{CORR} - E_E)\right\} * \text{Area}$ (7) |

All variables and constants are defined in Tables 3 and 4, respectively. Area means element area of copper surface in specific mesh.

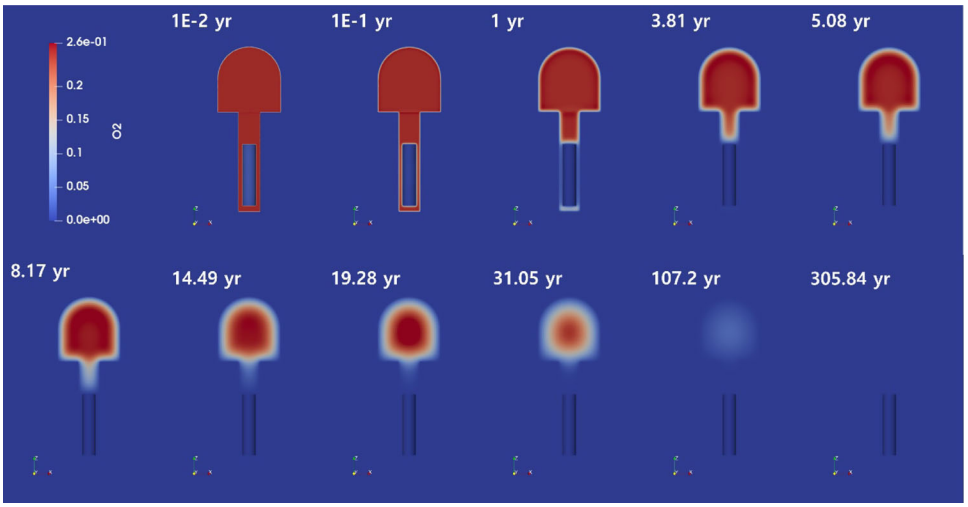


**Fig. 11 Concentration profile of $O_2$.** Distributions of $O_2$ in engineering barrier system (disposal turner, bentonite, and canister).

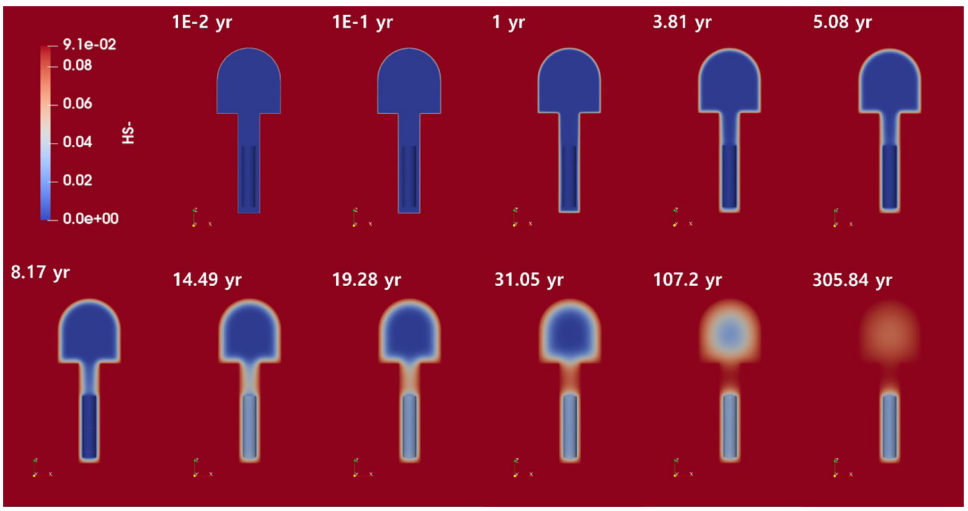


**Fig. 12 Concentration profile of $HS^-$.** Distributions of $HS^-$ in engineering barrier system (disposal turner, bentonite, and canister).

solution ($HS^-$ containing)[39,40]. In Fig. 10, the calculated corrosion potential is located between −0.05 to −0.40 $V_{SCE}$ for up to a half year. If considering $Cl^-$ concentration, then the corrosion potential cannot be over the pitting corrosion potential (−0.2 $V_{SCE}$) for the whole period of simulation. Therefore, the corrosion potential is not likely over the pitting corrosion potential and the canister surfaces are unlikely to corrode extensively through pitting.

Under the Cu sulfidation conditions (mixed oxic and anoxic, and anoxic corrosion), pitting corrosion is unlikely to occur. Even though, the Pilling–Bedworth (PB) ratio for the Cu-$Cu_2S$ interface is 1.93, it is unlikely having a passivation layer due to $Cu^+$ diffusion through the $Cu_2S$ layers and the results in Fig. 15[34,41]. Figure 15 shows that the high $Cl^-$ and $HS^-$ concentration ratios (>1000) hindered the formation of passivation films under the DGR simulated conditions, indicating that pitting corrosion was hindered under the simulated anoxic conditions. Furthermore, the current of Cu dissolution as $CuCl_2^-$ is negligibly small after 100 years in Fig. 13. However, because this is merely one simulated condition, lower $Cl^-$ and $HS^-$ concentration ratios should be simulated and considered in future studies.

## Fractures around engineering barriers: copper durability

The durability of the copper corrosion-resistant material was calculated based on the corrosion depth for the different canister surfaces, as shown in Fig. 16. The copper durability was determined as the point at which the corrosion depth reached the Cu canister thickness (i.e., 0.05 m). At the top and bottom canister surface edges, the expected Cu durability was the shortest, which was related to the $HS^-$ flux at the surface edges where the $HS^-$ was supplied not only radially but also axially.

As shown in Fig. 16, under harsh conditions (i.e., fractures surrounding the bentonite and tunnel), the durability of the copper corrosion-resistant material was sufficient to enable the radiotoxicity of the spent nuclear fuel (PWR) to fall below that of natural uranium ore. The radiotoxicity of the spent nuclear fuel should be lower than that of natural uranium ore after approximately 6E5 years, which is much sooner than the copper failure time (approximately 1.7E6 years). This result indicated that the engineering barrier system is sufficient for isolating and storing spent nuclear fuels in the determined conditions because by the time the copper corrosion-resistant material eventually fails, the radiotoxicity of the spent nuclear fuel is too low to cause any environmental damage.

## Highlights from model results

A multiphysics-based model was developed for predicting the long-term corrosion of Cu canisters for storing spent nuclear fuel in DGRs. The developed model was validated using corrosion data

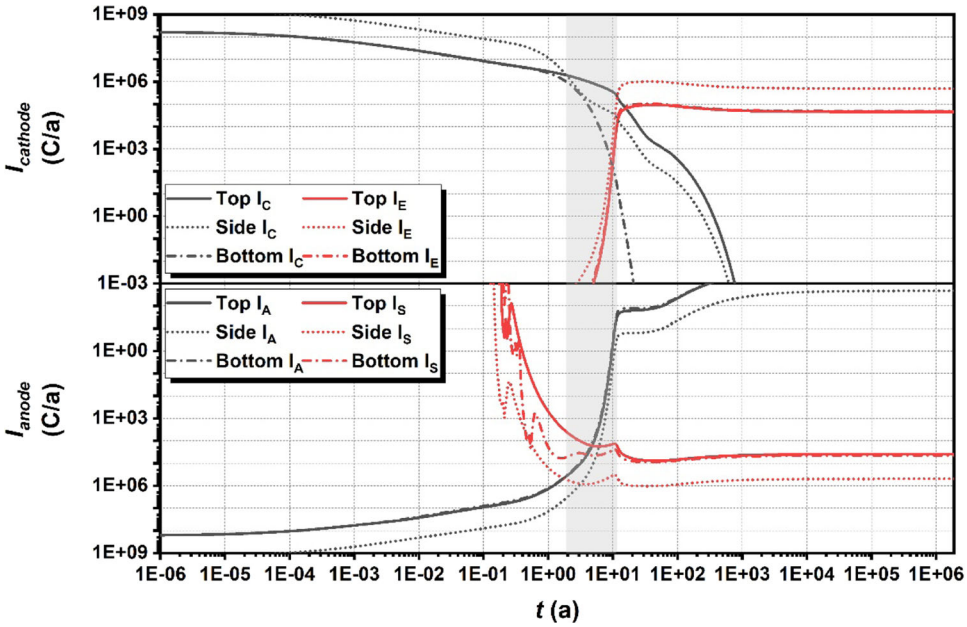


**Fig. 13 Cathodic ($I_{cathode}$) and anodic ($I_{anode}$) current densities for corrosion of copper top, side, and bottom surfaces.** $i_A$: anodic current density for anodic dissolution of Cu with $Cl^-$; $i_S$: anodic current density for Cu sulfidation; $i_C$: cathodic current density for $O_2$ reduction; $i_E$: cathodic current density for $H_2O$ reduction with $HS^-$.

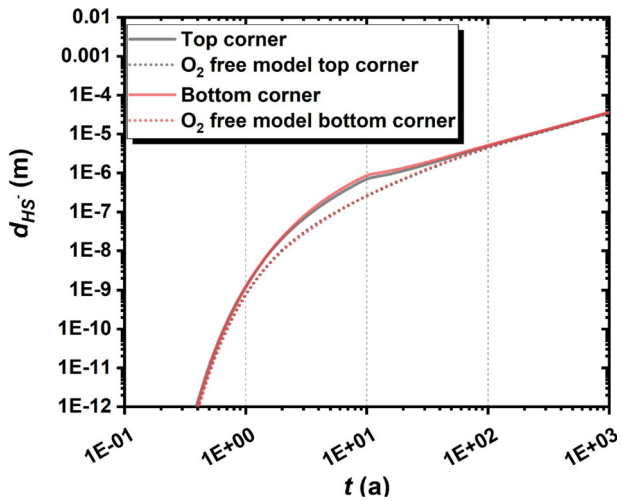


**Fig. 14 Corrosion depth evolution with time.** Corrosion depth ($d_{HS^-}$) at top and bottom corners of copper canister with and without $O_2$.

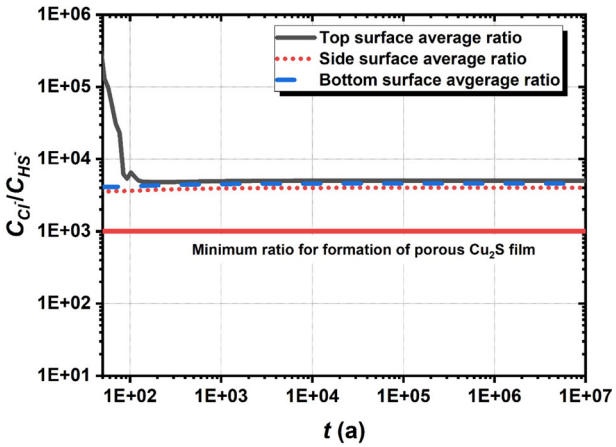


**Fig. 15 Ion ratio change with time evolution.** $Cl^-$ and $HS^-$ concentration ratios ($C_{Cl^-}/C_{HS^-}$) for Cu canister top, side, and bottom surfaces plotted as functions of time[61].

experimentally measured under anoxic conditions for optimizing the Cu canister durability in DGRs. By comparing the experimentally measured and numerically calculated results, the diffusion coefficient of $Cu^+$ ions in $Cu_2S$ films was determined as $3.6E-14\ m^2{\cdot}s^{-1}$, which agreed with previously reported experimentally measured $Cu^+$ diffusion coefficients[33]. By coupling mixed-potential theory and thermal hydraulics, the developed model predicted the corrosion potential and lifetime of Cu canisters in DGRs.

Our model showed that copper canisters corroded through the long-cell action under the environmental conditions in DGRs. Although the canister side surface corroded faster than the other surfaces up to 100 years, the long-cell action negligibly affected the canister corrosion owing to the limited $O_2$ content. Furthermore, owing to high $Cl^-$ and $HS^-$ concentration ratios ($Cl^-/HS^-$), the Cu canisters did not corrode through pitting in DGRs, which was validated using the numerical model. However, because this may not be true for lower $Cl^-$ and $HS^-$ concentration ratios, additional research must be conducted under lower $Cl^-$ and $HS^-$ conditions to determine whether localized pitting corrosion is possible.

The developed model showed that under harsh conditions such as fractures around the bentonite and tunnel, the engineering barrier of the KAERI reference disposal system maintained its functionality for isolating spent nuclear fuel until the radiotoxicity was reduced below that of natural uranium ore. The canister lifetime was at least one million years longer than the time required for the radiotoxicity of the spent nuclear fuel (PWR) to decay to that of natural uranium ore.

The proposed model will be improved by implementing important chemical reactions in corrosion processes under both oxic and anoxic conditions. In addition, although this 2-D model can be expanded to a 3-D one, the latter requires a huge

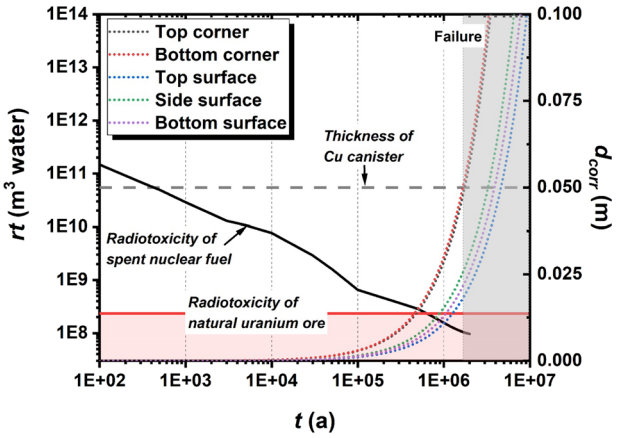


**Fig. 16 Corrosion depth and radiotoxicity change with time.** Cu corrosion depth ($d_{corr}$) and radiotoxicity (rt) of spent nuclear fuel (PWR) containing 55,000 MWD/MTU (4.5 wt.%)[62].

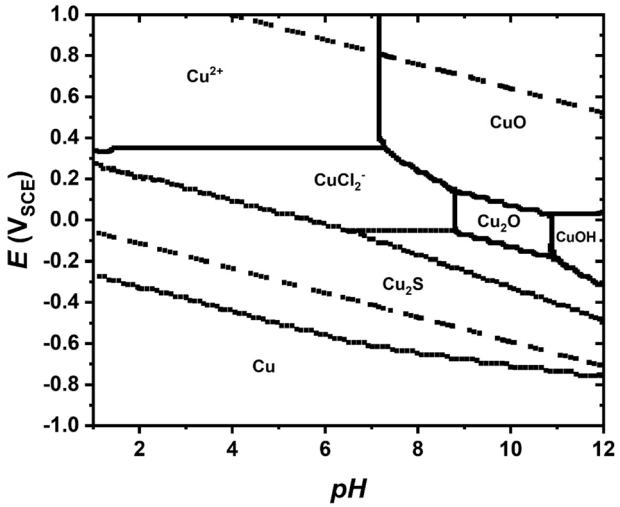


**Fig. 17 Pourbaix (Eh–pH equilibrium) diagram of Cu in DGR system.** Cu: 1E − 9 mol m$^{-3}$, $Na^+$: 0.1 mol m$^{-3}$, $Cl^-$: 0.1 mol m$^{-3}$, $HS^-$: 0.001 mol·m$^{-3}$, and $T = 25$ °C for simple Helgeson–Kirkham–Flowers activity coefficient model.

computational cost. Hence, the developed model will first implement the chemical reactions and then be optimized prior to expansion to a 3-D model, which should simultaneously simulate all the important corrosion process physics for DGRs.

## METHODS

### Model description

We used multiphysics object-oriented simulation environment (MOOSE) software to develop the multiphysics model for analyzing the long-term corrosion of copper canisters in granite host rock[42,43]. MOOSE uses the finite element method and portable, extensible toolkit for scientific computation (PETSc) as a solver for calculating numerical solutions for governing equations. Gmsh software was used for generating meshes so that elements mimicked DGR system geometries. After the calculations, ParaView software was used for extracting calculated data from the geometric elements. All the software are free, and MOOSE is open source.

### Nature of corrosion and model assumptions

Granite is a host rock candidate for DGR natural barriers in South Korea, Finland, and Sweden. In the DGR conditions, many different types of corrosion can happen, such as general corrosion, pitting corrosion, stress corrosion cracking, crevice corrosion, and radiation-induced corrosion. Among these corrosion processes, general corrosion by oxic and anoxic conditions is the dominant corrosion process[8,11,14]. The other processes cause less corrosion depth than the general corrosion process because of not sustainable environments for growing corrosion depth. Still, these corrosion processes cannot be ignored due to the geological time scale and must be evaluated by either experiment or modeling to get permission for the construction of DGR.

Especially, radiation-induced corrosion cases are studied a lot by researchers for several decades[11,26,44–52]. Still, the overall effect is not well known due to the complexity of radiation-induced electrochemical-chemical reactions in underground water. Many researchers try to understand the radiation-induced effects on the corrosion process by different methods. Recently, Inna et al. showed the radiation-induced corrosion of Cu in pure water is mainly due to $O_2$ instead of $H_2O_2$ or OH· through an experiment and simple model of radiation-induced corrosion of Cu[26]. Also, Morco et al. suggest a model of radiation-induced corrosion of Cu conservatively[53].

In our developed model, the authors focused on the development of Cu corrosion under oxic and anoxic conditions by $O_2$, $Cl^-$, and $HS^-$, which are the predominant chemical species affecting Cu corrosion in granite host rock[6,14]. For the radiation-induced corrosion of Cu, the authors consider it as a future plan to develop corrosion modeling; because the radiolysis of groundwater includes complicated reactions, and also the radiolysis of groundwater generates $H_2$[54–57]. This generated $H_2$ can react with minerals in bentonite and backfill materials (such as montmorillonite, calcite, siderite. pyrite, and gypsum) and the overall effect must consider the bentonite behavior[44,58,59]. Therefore, the expected effects of dissolved $H_2$ on Cu corrosion must incorporate various phenomena that this developed model cannot handle until now.

The corrosion of Cu can be induced by $O_2$ and $HS^-$ under oxic and anoxic conditions, respectively. Because oxidized Cu can combine with $Cl^-$ ions and dissolve into groundwater as Cu–Cl complexes[6,14]. The influences of $O_2$, $Cl^-$, and $HS^-$ were considered for anodic, cathodic, and dissolution reactions at the Cu–bentonite interface, respectively. Based on a chemical speciation calculation, $Cu_2S$ was selected as the most stable chemical Cu species in the model. The chemical speciations were calculated using Spana software (developed by KTH), and the results were plotted as the corresponding Pourbaix diagram (Fig. 17). DGRs should be constructed at least 500 m underground, where conditions are anoxic and the corresponding electron activity ($E_h$) is between −0.4 and −0.7 $V_{SHE}$ [vs. a standard hydrogen electrode (SHE)]. In addition, groundwater pH is alkaline, and bentonite will buffer pH in the range 8–9. As shown in Fig. 17, $Cu_2S$ is the most stable form of Cu in these pH and Eh ranges.

### Model formula

Figure 18 shows a schematic of the coupled mixed-potential and thermal hydraulics MOOSE-based time transient model. In the numerical model, the Cu corrosion potential is first determined by the initial condition and inner iterations by adjusting the anodic and cathodic current densities at the Cu–bentonite interface, and the corrosion potential then updates the Neumann boundary conditions of the chemical species. These boundary condition updates change the reaction rates of the chemical species, which participate in Cu corrosion through electrochemical reactions, at the Cu–bentonite interface. Then, the updated boundary conditions are used to couple the thermal hydraulics and reactive transportation physics and find a numerical solution for the geometry. If the solution does not converge, the entire process is repeated by calculating the corrosion potential at the specific time. The numerical solution for this timestep then becomes the

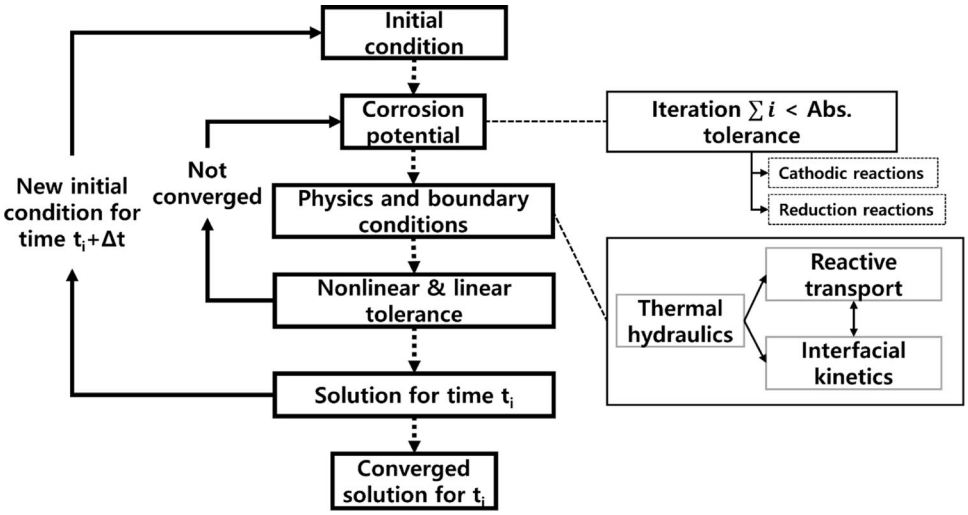


**Fig. 18 Logic of developed numerical model.** Schematic showing flow of mixed-potential model for calculating numerical solutions.

**Table 3.** Definition of variables used in this model.

| Symbol | Definition | Unit |
|---|---|---|
| $T$ | Temperature | K |
| $C_1$ | $Cl^-$ | mol $m^{-3}$ |
| $C_2$ | $HS^-$ | mol $m^{-3}$ |
| $C_3$ | $O_2$ | mol $m^{-3}$ |
| $C_4$ | $Cu^{2+}$ | mol $m^{-3}$ |
| $C_5$ | $CuCl_2^-$ | mol $m^{-3}$ |
| $i_A$ | Anodic current of reaction A | C $a^{-1}$ |
| $i_B$ | Anodic current of reaction B | C $a^{-1}$ |
| $i_C$ | Cathodic current of reaction C | C $a^{-1}$ |
| $i_D$ | Cathodic current of reaction D | C $a^{-1}$ |
| $i_E$ | Cathodic current of reaction E | C $a^{-1}$ |
| $E_{corr}$ | Corrosion Potential [*vs.* saturated calomel electrode (SCE)] | $V_{SCE}$ |

updated initial condition for finding a numerical solution for the next time step.

### Mixed-potential boundary conditions

The mixed-potential equations were adopted from the CSM, and a Jacobian was derived for calculating Cu corrosion under oxic and anoxic conditions[20]. The corrosion potentials of Cu and copper surfaces at time $t_i$ can be calculated using Eq. (3) as follows:

$$i_A + i_B + i_C + i_E = 0, \tag{3}$$

where $i_A$ is the anodic current [C·$a^{-1}$] of the Cu dissolution under oxic conditions with the presence of $Cl^-$ to form $CuCl_2^-$, $i_B$ is the anodic current [C·$a^{-1}$] of the Cu sulfidation (including anodic dissolution) by $HS^-$ to form $Cu_2S$, $i_C$ is the cathodic current [C·$a^{-1}$] of the $O_2$ cathodic reduction, and $i_E$ is the cathodic current [C·$a^{-1}$] of the water cathodic reduction by $HS^-$. In this numerical model, positive and negative represent anodic and cathodic currents, respectively. All the electrochemical and corresponding Butler–Volmer reactions are defined in Table 2 (Tables 3 and 4—summary of the terms). Although the corrosion potential can be calculated by substituting Eqs. (4)–(7) in Table 2 into Eq. (3), the numerical solution is not analytical.

In Eq. (3), each current term includes corrosion potential ($E_{corr}$) as can be seen in Table 2. This Eq. (3) cannot have an exact solution for corrosion potential, because Eq. (3) has three more variables which are the concentration of $O_2$, $Cl^-$, and HS. These three variables depend on the transportation of chemical species through diffusion and thermal hydraulics. Therefore, it is impossible to get an exact solution from Eq. (3). Therefore, an iterative method (Fig. 19) was implemented to calculate corrosion potential for corresponding timesteps.

The corrosion potential numerical solution was iteratively calculated, as shown in Fig. 19. The sum of the overall currents approached to zero on the entire copper canister surface. If the sum of the redox currents was above the tolerance ($\delta$), which is

**Table 4.** Definition of parameters and corresponding values used in this model.

| Symbol | Definition | Value | Unit |
|---|---|---|---|
| $F$ | Faraday constant | 96485 | C $mol^{-1}$ |
| $R$ | Gas constant | 8.314 | J $(mol{\cdot}K)^{-1}$ |
| $n_A$ | Number of electrons participating in reaction A | 1 | - |
| $n_B$ | Number of electrons participating in reaction B | 1 | - |
| $n_C$ | Number of electrons participating in reaction C | 1 | - |
| $n_E$ | Number of electrons participating in reaction E | 4 | - |
| $k_A$ | Rate constant of reaction A | 1.04 | $m^4(mol{\cdot}a)$ |
| $k_{AB}$ | Rate constant of reversed reaction A | 4.48E3 | m $a^{-1}$ |
| $k_B$ | Rate constant of reaction B | 1.89E6 | $m^4(mol{\cdot}a)$ |
| $k_C$ | Rate constant of reaction C | 5.63E − 3 | m $s^{-1}$ |
| $k_E$ | Rate constant of reaction E | 6.31E − 2 | m $s^{-1}$ |
| $E_A$ | Standard potential of reaction A | −0.105 | $V_{SCE}$ |
| $E_{B1}$ | Standard potential of reaction B1 | −0.747 | $V_{SCE}$ |
| $E_{B2}$ | Standard potential of reaction B2 | −0.747 | $V_{SCE}$ |
| $E_C$ | Standard potential of reaction C | 0.16 | $V_{SCE}$ |
| $E_E$ | Standard potential of reaction E | −1.005 | $V_{SCE}$ |
| $\alpha_{B1}$ | Transfer coefficient of reaction B1 | 0.5 | – |
| $\alpha_{B2}$ | Transfer coefficient of reaction B2 | 0.5 | – |
| $\alpha_C$ | Transfer coefficient of reaction C | 0.37 | – |
| $\alpha_E$ | Transfer coefficient of reaction E | 0.5 | – |

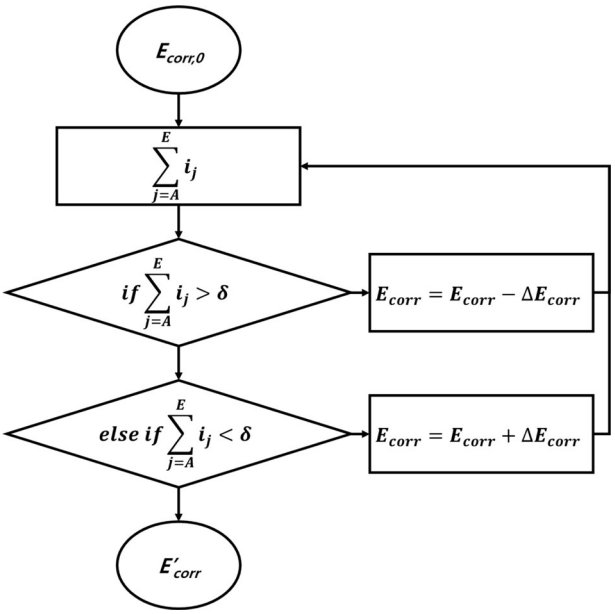


**Fig. 19 Logic for calculating corrosion potential in the developed model.** Schematic showing flow of numerical iterations for finding corrosion potential at specific condition and time step.

the criterion for numerical solution convergence, then the corrosion potential was reduced to minimize the difference between the anodic and cathodic currents. In contrast, if the sum of the redox currents was below δ then the corrosion potential was increased to reduce the difference between the anodic and cathodic currents. The tolerance (δ) was set to 10 C·a$^{-1}$ because the 10 C·a$^{-1}$ means no more than 10 number of copper atoms can be corroded more than the numerically calculated corrosion results for the entire surface of the canister per year. Therefore, not even a single layer molecular layer (10 number of Cu atoms on a Cu canister surface) of copper can be corroded by the numerical error, thus 10 C·a$^{-1}$ value is negligibly small and cannot contribute to the overall corroded depth of the copper canister.

At the beginning of the numerical calculation, the corrosion potential ($E_{corr,0}$) was set as zero or the corrosion potential of the previous time step and started to do iteration as in Fig. 19 to calculate the correct corrosion potential ($E'_{corr}$) at the given time step. The corrosion potential is calculated based on Eq. (3) and initial conditions to set the boundary conditions for thermal-hydraulics. After that, the coupled thermal-hydraulics and interface kinetics are solved by using the boundary conditions and the corrosion potential. Then, the thermal-hydraulics updated the concentration of $O_2$, $Cl^-$, $HS^-$, and temperature which was used for recalculating the corrosion potential. These processes repeat in the single time step until the non-linear relative tolerance meets the criteria of the simulation. Once the thermal hydraulics and corrosion potentials were solved in the present time step, then the concentrations of $O_2$, $Cl^-$, $HS^-$, temperature, and the corrosion potential ($E'_{corr}$ in Fig. 19) will be the initial conditions for the next time step.

### Fluid mass transportation

The MOOSE porous flow module was used to simulate thermal hydraulics in porous media for the coupled mixed-potential and thermal hydraulics model[43]. A governing equation (Eq. (8)), which is the law of mass conservation, was adopted for fluid flow in porous media.

$$\frac{\partial M}{\partial t} = \nabla \cdot \left(\rho \frac{k}{\mu}(\nabla P - \rho g)\right), \tag{8}$$

where $M$ is the mass density of the fluid [kg·m$^{-3}$], $\rho$ is the fluid density [kg·m$^{-3}$], $k$ is the porous medium (bentonite and backfill) permeability [m$^2$], $\mu$ is the fluid viscosity [N·m$^{-2}$ a$^{-1}$], $P$ is the porous medium pore pressure [Pa], and $g$ is the gravitational acceleration [m·s$^{-2}$]. The first term $(\frac{\partial M}{\partial t})$ in Eq. (8) represents the mass change over time, and the second term $(\nabla \cdot (\rho \frac{k}{\mu}(\nabla P - \rho g)))$ represents fluid advection through Darcy flow in porous media. Equation (8) was implemented to calculate the bentonite and backfill material pore pressures, which were used with the van Genuchten equation (for the capillary pressure–saturation relationship) (Eq. (9)) to calculate the saturation degree as follows:

$$\text{if P<0, } S = \left(1 + (-aP)^{\frac{1}{(1-m)^{-m}}}\right)^{-m},$$

$$\text{else if P } \geq 0, S = 1, \tag{9}$$

where $a$ and $m$ are (dimensionless) van Genuchten parameters. The calculated (dimensionless) saturation degree ($S$) was coupled to both chemical species and heat transportations in porous media (e.g., the bentonite and backfill material).

### Transportation of chemical species

Because the transportation of chemical species plays an important role in the corrosion of Cu canisters in DGRs, Eq. (10) was used to calculate the transportation of chemical species as follows:

$$\phi \frac{\partial (SC_i)}{\partial t} = \nabla \cdot (\rho \phi \tau D_i \nabla C_i) + \nabla \cdot (vC_i), \tag{10}$$

where $S$ is the (dimensionless) saturation degree of porous media (e.g., bentonite and backfill), $\rho$ is the fluid density [kg·m$^{-3}$], $\phi$ is the (dimensionless) porous medium porosity, $\tau$ is the (dimensionless) porous medium tortuosity, $D_i$ is the diffusion coefficient of chemical species $i$ in the fluid [m$^2$·a$^{-1}$], $C_i$ is the concentration of chemical species $i$ [mol·m$^{-3}$], and $v$ is the Darcy velocity [m·s$^{-1}$]. In the governing equation (Eq. (10)), $\nabla \cdot (\rho \phi \tau D_i \nabla C_i)$ and $\nabla \cdot (vC_i)$ describe mass transportation through diffusion and Darcy flow, respectively. The diffusion term $(\nabla \cdot (\rho \phi \tau D_i \nabla C_i))$ was coupled to temperature through the Arrhenius equation (Eq. (11)) as follows:

$$D_i = D_{i,0} \exp\left(-\frac{E_{a,i}}{RT}\right), \tag{11}$$

where $D_{i,0}$ is the frequency factor [m$^2$·a$^{-1}$], $E_{a,i}$ is the activation energy of chemical species $i$ [J·mol$^{-1}$], $R$ is the gas constant [J·mol$^{-1}$·K$^{-1}$], and $T$ is the temperature of the target system [K]. The third term $(\nabla \cdot (vC_i))$ in Eq. (10) was coupled to the fluid mass transportation through the Darcy velocity ($v$), which can be calculated using Eq. (12) as follows:

$$v = \frac{k}{\mu}(\nabla P - \rho g), \tag{12}$$

which includes Eq. (8) and represents the fluid velocity in porous media (e.g., bentonite and backfill).

### Heat transfer

Heat energy conservation is the principle of the governing equation of heat continuity:

$$\frac{\partial \epsilon}{\partial t} = -\nabla \cdot (-\lambda \nabla T) - \nabla \cdot hF, \tag{13}$$

where $\epsilon$ is the amount of heat energy in the porous medium or target system [J·m$^{-3}$], $\lambda$ is the thermal conductivity of the porous medium or target system [W·m$^{-1}$·K$^{-1}$], $h$ is the specific enthalpy of a single phase (e.g., solution or porous fluid) [J·kg$^{-1}$], and $F$ is the

advective Darcy flux of a porous fluid [m·a$^{-1}$], which can be calculated using the $\nabla \cdot \{\rho \frac{k}{\mu}(\nabla P - \rho g)\}$ term in Eq. (8). In the governing equation (Eq. (13)), $\nabla \cdot (-\lambda \nabla T)$ and $\nabla \cdot hF$ represent heat conduction and convection in porous media or solutions. The heat transfer equation (Eq. (13)) was coupled to porous flow through the $\nabla \cdot hF$ term, which represents heat energy moving through Darcy flow in the solution, and can be applied to not only porous media but also stagnant liquids. The heat energy ($\epsilon$) in Eq. (13) is calculated using Eq. (14) as follows:

$$\epsilon = (1-\phi)\rho_{solid}c_{solid}T + \phi S\rho_{liquid}c_{liquid}T, \quad (14)$$

where $\phi$ is the (dimensionless) porous medium porosity, $\rho_{solid}$ is the (dimensionless) density of the solid part in the porous medium, $c_{solid}$ is the heat capacity of the solid part in the porous medium [J·kg$^{-1}$ K$^{-1}$], $c_{liquid}$ is the heat capacity of the liquid in the porous medium [J·kg$^{-1}$ K$^{-1}$], and $T$ is the system temperature [K].

## Experimental model validation

The numerical model was validated using two experimentally measured data sets by Smith et al.[31,32] and Chen et al.[29]. The first dataset was designed to compare the effects of the sulfide ion concentration on the copper corrosion potential by varying the sulfide ion concentration in the solution. The second dataset was used for checking the Cu corrosion in sulfide and chloride solutions through the corrosion potentials and total corroded Cu amounts.

For the first model validation dataset, 0-D geometry was assumed owing to the lack of information about the experiment[32]. Smith et al. purged a very low-oxygen-concentration 0.1 M chloride solution with argon gas before the experiments[32]. During the experiments, certain sulfide solution concentrations were added to the solution, and the Cu corrosion potentials were measured. The details of the $O_2$ and $HS^-$ concentrations in the solution are given in section "Methods".

For the second validation dataset, a 2-D geometric model was used to simplify the experimental geometry and reduce the computational cost. Chen et al. (2010 and 2017) anoxically corroded Cu in solutions containing different sulfide and chloride concentrations[29,30]. Coin-shaped Cu specimens (⌀1 cm) were stored up to 1750 h in 1 L of solution containing a mixture of sulfide and chloride ions. Figure 3 shows the simplified 2-D geometries and meshes of the solution and Cu specimen surfaces assigned as a surface and lines, respectively.

The electrochemical boundary conditions given by Eqs. (4)–(7) in Table 2 were assigned to the top surface of the copper specimen (Fig. 3). In the model, a zero flux was assigned to the copper specimen side surface, which was coated with a nonconductive lacquer in the experiments[29,30]. The initial domain (solution) temperature was set to 25 °C and remained constant during the entire calculation (Table 5), and 1 mM and 0.1 M $Cl^-$ solutions were applied as the domain[29,30]. A film growth model and a without film growth model were implemented for comparing the effects of $Cu_2S$ film on the corrosion of Cu.

**Table 5.** Initial temperature and diffusion coefficients[29].

| Initial temperature | | | |
|---|---|---|---|
| $T$ | 298.15 K | | |
| Diffusion coefficients | | | |
| $D_{HS^-}$ | $5E-10$ m$^2$ s$^{-1}$ | $D_{Cl^-}$ | $2E-9$ m$^2$ s$^{-1}$ |
| $D_{CuCl2^-}$ | $6E-10$ m$^2$ s$^{-1}$ | $O_2$ | $2.4E-9$ m$^2$ s$^{-1}$ |

## Deep geological repository

Figure 20 presents the geometry of the KAERI reference disposal unit for the pressurized water reactor (PWR) spent-nuclear-fuel DGR. Also, Fig. 20 show the 2-D geometry of the numerical model for simulating the axisymmetrically shaped KAERI reference disposal unit exhibiting 40- and 8-m disposal and canister spacings, respectively. KJ-II bentonite was selected for the disposal hole bentonite blocks and tunnel backfill materials[60]. Copper was chosen as the corrosion-resistant material for the 5-cm-thick spent-nuclear-fuel canisters. Granite host rock was selected for the natural barrier system around the disposal holes and tunnels. The details of the barrier system physical properties and initial conditions are provided in Supplementary Methods.

To simplify and reduce the computational cost, only 100 m of host rock was modeled in the geometry (Fig. 20). The 40- and 8-m tunnel and canister spacings were applied to a 10.09-m wide host rock exhibiting a volume equivalent to those of the 40- and 8-m tunnel and canister spacings for a single canister, respectively.

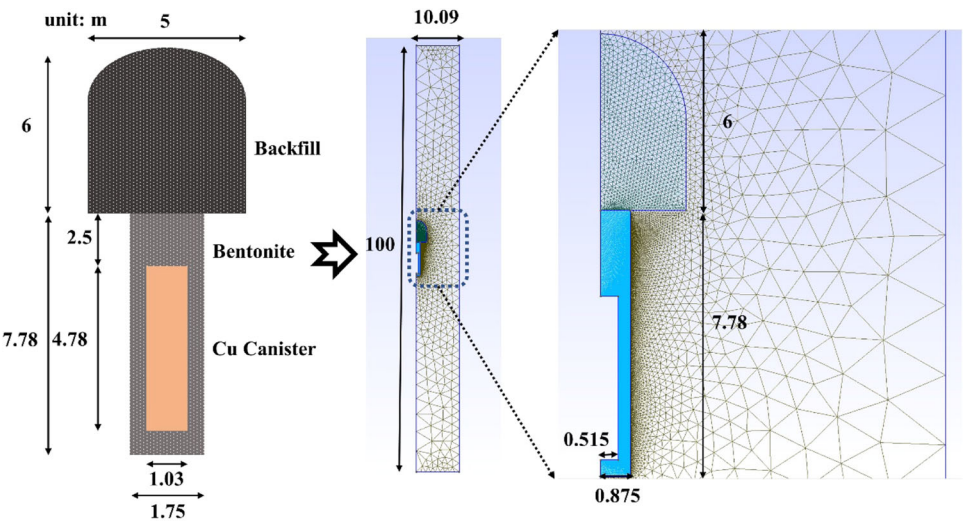


**Fig. 20 Simplified geometry of deep geological repository.** KAERI reference disposal unit, 2-D geometry of numerical model, and geometry of expanded around engineering barriers.

## DATA AVAILABILITY

The data that support the findings of this study are available from the corresponding author upon reasonable request.

## CODE AVAILABILITY

The underlying code for this study validation datasets is not publicly available but may be made available to qualified researchers on reasonable request from the corresponding author.

Received: 5 October 2022; Accepted: 20 March 2023;
Published online: 08 April 2023

## REFERENCES

1. Park, B.-H., Gao, F., Kwon, E.-H. & Ko, W.-I. Comparative study of different nuclear fuel cycle options: quantitative analysis on material flow. *Energy Pol.* **39**, 6916–6924 (2011).
2. Nuclear Energy Agency. Strategies and considerations for the back end of the fuel cycle. OECD-NEA Report No. 7469 (2021).
3. Bodansky, D. *Nuclear Energy: Principles, Practices, and Prospects* 2nd edn (Springer, 2005).
4. Crossland, I. in *Nuclear Fuel Cycle Science and Engineering* 531–557 (Woodhead Publishing, 2012).
5. Nuclear Energy Agency. Advanced nuclear fuel cycles and radioactive waste management. OECD-NEA Report No. 5990 (NEA, 2006).
6. European Commision. State of the art document on the corrosion behaviour of container materials. COBECOMA (2004).
7. Lawrence Livermore National Lab. Evaluation of copper, aluminum bronze, and copper-nickel container material for the Yucca mountain project. UCRL-101097 (1989).
8. King, F., Hall, D. S. & Keech, P. G. Nature of the near-field environment in a deep geological repository and the implications for the corrosion behaviour of the container. *Corros. Eng. Sci. Technol.* **52**, 25–30 (2017).
9. Wang, J., Chen, L., Su, R. & Zhao, X. The Beishan underground research laboratory for geological disposal of high-level radioactive waste in China: planning, site selection, site characterization and in situ tests. *J. Rock Mech. Geotech. Eng.* **10**, 411–435 (2018).
10. Guo, M. The electrochemical and corrosion study of copper for nuclear waste containers under deep geological disposal conditions. Electronic Thesis and Dissertation Repository 7371, The University of Western Ontario (2020).
11. Hall, D. S., Behazin, M., Binns, W. J. & Keech, P. G. An evaluation of corrosion processes affecting copper-coated nuclear waste containers in a deep geological repository. *Prog. Mater. Sci.* **118**, 100766 (2021).
12. Choi, H.-J., Lee, J.-Y. & Choi, J. Development of geological disposal systems for spent fuels and high-level radioactive wastes in korea. *Nucl. Eng. Technol.* **45**, 29–40 (2013).
13. Svensk kärnbränslehantering AB. Beräkning av nuklidinnehåll, resteffekt, aktivitet samt doshastighet för utbränt kärnbränsle. SKB-R-99-74 (2000).
14. Svensk kärnbränslehantering AB. An update of the state-of-the-art report on the corrosion of copper under expected conditions in a deep geologic repository. SKB-TR-10-67 (2010).
15. Uhlig, H. H. Initial oxidation rate of metals and the logarithmic equation. *Acta Metall.* **4**, 541–554 (1956).
16. King, F. A natural analogue for the long-term corrosion of copper nuclear waste containers-reanalysis of a study of a bronze cannon. *Appl. Geochem.* **10**, 477–487 (1995).
17. Svensk kärnbränslehantering AB. A natural analogue for copper waste canisters: The copper-uranium mineralised concretions in the Permian mudrocks of south Devon, United Kingdom. SKB-TR-00-11 (2000).
18. Perea, N. M. A natural analogue for copper canisters. *MRS Online Proc. Libr.* **465**, 1153–1160 (1996).
19. Moinuddin, M. *Comsol Modelling of Uniform Corrosion of Used Nuclear Fuel Canisters* (York University, 2018).
20. Posiva Oy. Mixed-potential modelling of the corrosion of copper in the presence of sulphide. Working Report 2007-63. (2008).
21. Briggs, S., McKelvie, J., Keech, P., Sleep, B. & Krol, M. Transient modelling of sulphide diffusion under conditions typical of a deep geological repository. *Corros. Eng. Sci. Technol.* **52**, 200–203 (2017).
22. Briggs, S., McKelvie, J., Sleep, B. & Krol, M. Multi-dimensional transport modelling of corrosive agents through a bentonite buffer in a Canadian deep geological repository. *Sci. Total Environ.* **599–600**, 348–354 (2017).
23. Rolle, M., Sprocati, R., Masi, M., Jin, B. & Muniruzzaman, M. Nernst-Planck-based description of transport, Coulombic interactions, and geochemical reactions in porous media: modeling approach and benchmark experiments. *Water Resour. Res.* **54**, 3176–3195 (2018).
24. Rashwan, T. L. et al. Exploring the governing transport mechanisms of corrosive agents in a Canadian deep geological repository. *Sci. Total Environ.* **828**, 153944 (2022).
25. Zhang, F. et al. Corrosion-induced microstructure degradation of copper in sulfide-containing simulated anoxic groundwater studied by synchrotron high-energy X-ray diffraction and ab-initio density functional theory calculation. *Corros. Sci.* **184**, 109390 (2021).
26. Soroka, I., Chae, N. & Jonsson, M. On the mechanism of γ-radiation-induced corrosion of copper in water. *Corros. Sci.* **182**, 109279 (2021).
27. King, F., Litke, C. D. & Ryan, S. R. A mechanistic study of the uniform corrosion of copper in compacted Na-montmorillonite/s and mixtures. *Corros. Sci.* **33**, 1979–1995 (1992).
28. Morikawa, M., Ahmed, N., Yoshida, Y. & Izumi, Y. Photoconversion of carbon dioxide in zinc-copper-gallium layered double hydroxides: the kinetics to hydrogen carbonate and further to CO/methanol. *Appl. Catal. B Environ.* **144**, 561–569 (2014).
29. Chen, J., Qin, Z. & Shoesmith, D. W. Kinetics of corrosion film growth on copper in neutral chloride solutions containing small concentrations of sulfide. *J. Electrochem. Soc.* **157**, C338 (2010).
30. Chen, J., Qin, Z., Martino, T. & Shoesmith, D. W. Effect of chloride on Cu corrosion in anaerobic sulphide solutions. *Corros. Eng. Sci. Technol.* **52**, 40–44 (2017).
31. Smith, J. M., Wren, J. C., Odziemkowski, M. & Shoesmith, D. W. The electrochemical response of preoxidized copper in aqueous sulfide solutions. *J. Electrochem. Soc.* **154**, C431 (2007).
32. Smith, J., Qin, Z., King, F., Werme, L. & Shoesmith, D. W. Sulfide film formation on copper under electrochemical and natural corrosion conditions. *Corrosion* **63**, 135–144 (2007).
33. Cassaignon, S., Pauporté, T., Guillemoles, J. F. & Vedel, J. Copper diffusion in copper sulfide: a systematic study. *Ionics* **4**, 364–371 (1998).
34. Chen, J., Qin, Z. & Shoesmith, D. W. Copper corrosion in aqueous sulfide solutions under nuclear waste repository conditions. *MRS Online Proc. Libr.* **1475**, 465–470 (2012).
35. Lee, C., Cho, W.-J., Lee, J. & Kim, G.-Y. Numerical analysis of coupled thermo-hydro-mechanical (THM) behavior at Korean Reference Disposal System (KRS) using TOUGH2-MP/FLAC3D simulator. *J. Nucl. Fuel Cycle Waste Technol.* **17**, 183–202 (2019).
36. Lee, C., Lee, J., Kim, G.-Y. & Kim, M. Implementation of Barcelona Basic Model into TOUGH2-MP/FLAC3D. *Tunn. Undergr. Sp.* **30**, 39–62 (2020).
37. King, F., Chen, J., Qin, Z., Shoesmith, D. & Lilja, C. Sulphide-transport control of the corrosion of copper canisters. *Corros. Eng. Sci. Technol.* **52**, 210–216 (2017).
38. Allah, A. G. G., Abou-Romia, M. M., Badawy, W. A. & Rehan, H. H. Effect of halide ions on passivation and pitting corrosion of copper in alkaline solutions. *Mater. Corros.* **42**, 584–591 (1991).
39. Guo, M. et al. The susceptibility of copper to pitting corrosion in borate-buffered aqueous solutions containing chloride and sulfide. *J. Electrochem. Soc.* **166**, C550 (2019).
40. Mao, F., Dong, C. S. S.-A., Lu, P. & Macdonald, D. D. Passivity breakdown on copper: influence of chloride ion. *Electrochim. Acta* **144**, 391–399 (2014).
41. Stenlid, J. H., Santos, E. C. D., Johansson, A. J. & Pettersson, L. G. M. Properties of interfaces between copper and copper sulphide/oxide films. *Corros. Sci.* **183**, 109313 (2021).
42. Permann, C. J. et al. MOOSE: enabling massively parallel multiphysics simulation. *SoftwareX.* **11**, 100430 (2020).
43. Wilkins, A., Green, C. P. & Ennis-King, J. An open-source multiphysics simulation code for coupled problems in porous media. *Comput. Geosci.* **154**, 104820 (2021).
44. King, F. & Behazin, M. A review of the effect of irradiation on the corrosion of copper-coated used fuel containers. *Corros. Mater. Degrad.* **2**, 678–707 (2021).
45. Feron, D. in *Nuclear Corrosion Science and Engineering* 31–56 (Woodhead Publishing, 2012).
46. Ershov, B. G. & Gordeev, A. V. A model for radiolysis of water and aqueous solutions of $H_2$, $H_2O_2$ and $O_2$. *Radiat. Phys. Chem.* **77**, 928–935 (2008).
47. Spinks, J. W. T. & Woods, R. J. *An Introduction to Radiation Chemistry* (Wiley, 1990).
48. Björkbacka, Å., Hosseinpour, S., Johnson, M., Leygraf, C. & Jonsson, M. Radiation induced corrosion of copper for spent nuclear fuel storage. *Radiat. Phys. Chem.* **92**, 80–86 (2013).
49. Lousada, C. et al. Gamma radiation induces hydrogen absorption by copper in water. *Sci. Rep.* **6**, 1–8 (2016).
50. Bessho, K. et al. Corrosion of copper in water and colloid formation under intense radiation field. *J. Radioanal. Nucl. Chem.* **303**, 1117–1121 (2015).

51. Björkbacka, Å., Johnson, C. M., Leygraf, C. & Jonsson, M. Role of the oxide layer in radiation-induced corrosion of copper in anoxic water. *J. Phys. Chem. C* **120**, 11450–11455 (2016).
52. Daub, K., Zhang, X., Noël, J. J. & Wren, J. C. Gamma-radiation-induced corrosion of carbon steel in neutral and mildly basic water at 150 °C. *Corros. Sci.* **53**, 11–16 (2011).
53. Morco, R. P. et al. Modelling of radiolytic production of $HNO_3$ relevant to corrosion of a used fuel container in deep geologic repository environments. *Corros. Eng. Sci. Technol.* **52**, 141–147 (2017).
54. Henshaw, J. et al. A model of chemistry and thermal hydraulics in PWR fuel crud deposits. *J. Nucl. Mater.* **353**, 1–11 (2006).
55. Buxton, G. V., Greenstock, C. L., Helman, W. P. & Ross, A. B. Critical review of rate constants for reactions of hydrated electrons, hydrogen atoms and hydroxyl radicals (·OH/·O− in aqueous solution. *J. Phys. Chem.* **17**, 513–886 (1988).
56. Elliot, A. J. & McCracken, D. R. Computer modelling of the radiolysis in an aqueous lithium salt blanket: suppression of radiolysis by addition of hydrogen. *Fusion Eng. Des.* **13**, 21–27 (1990).
57. Caër, S. L. Water radiolysis: influence of oxide surfaces on $H_2$ production under ionizing radiation. *Water* **3**, 235–253 (2011).
58. Kaufhold, S., Dohrmann, R., Koch, D. & Houben, G. The pH of aqueous bentonite suspensions. *Clays Clay Miner.* **56**, 338–343 (2008).
59. Michael, J. & Ahn, J. in *Geological Repository Systems for Safe Disposal of Spent Nuclear Fuels and Radioactive Waste* Ch. 12 (Woodhead Publishing, 2017).
60. Yoo, M., Choi, H.-J., Lee, M. & Lee, S. Measurement of properties of domestic bentonite for a buffer of an HLW Repository. *J. Nucl. Fuel Cycle Waste Technol.* **14**, 135–147 (2016).
61. Chen, J., Qin, Z. & Shoesmith, D. W. Key parameters determining structure and properties of sulphide films formed on copper corroding in anoxic sulphide solutions. *Corros. Eng. Sci. Technol.* **49**, 415–419 (2014).
62. Koplik, C. M., Kaplan, M. F. & Ross, B. The safety of repositories for highly radioactive wastes. *Rev. Mod. Phys.* **54**, 269–310 (1982).

## ACKNOWLEDGEMENTS

This research was supported by the Institute for Korea Spent Nuclear Fuel (iKSNF) through the National Research Foundation of Korea (NRF) funded by the Ministry of Science and ICT (NRF-2021M2E1A1085194) and the Korea Institute of Energy Technology Evaluation and Planning (KETEP) and the Ministry of Trade, Industry & Energy (MOTIE) of the Republic of Korea (No. 20224000000120).

## AUTHOR CONTRIBUTIONS

N.C. developed the model and wrote the original draft. S.P. conducted the data curation and wrote the original draft. S.S. visualized the data. R.I.F. and H.J. reviewed and edited the original draft. S.C. supervised the research and reviewed and edited the original draft.

## COMPETING INTERESTS

The authors declare no competing interests.

## ADDITIONAL INFORMATION

**Supplementary information** The online version contains supplementary material available at https://doi.org/10.1038/s41529-023-00345-6.

**Correspondence** and requests for materials should be addressed to Sungyeol Choi.

**Reprints and permission information** is available at http://www.nature.com/reprints

**Publisher's note** Springer Nature remains neutral with regard to jurisdictional claims in published maps and institutional affiliations.